Dark-field X-ray microscopy with structured illumination for three-dimensional imaging

Check for updates

Doğa Gürsoy [1 ✉], Kaan Alp Yay [2,3,4], Elliot Kisiel [1,5], Michael Wojcik [1], Dina Sheyfer [1], Arndt Last [6], Matthew Highland[1], Ian Randal Fisher [3,4,7], Stephan Hruszkewycz [8] & Zahir Islam[1 ✉]

Dark-field X-ray microscopy is a lens-based technique that enables real-space imaging of heterogeneous micro- and meso-scale ordered materials. However, achieving accurate three-dimensional (3D) reconstruction often requires meticulous sample alignment or rastering, requiring complex rotational setups and extended acquisition times. To address these challenges, we introduce a structured illumination technique optimized for 3D imaging of ordered materials at sub-micrometer length scales. Our approach employs a coded aperture to spatially modulate the incident X-ray beam, enabling 3D structural reconstruction from images captured at various aperture positions. Unlike current 3D imaging approaches, which often rely on rotational or rastering methods, our technique uses scanning X-ray silhouettes of the coded aperture for depth resolution along the diffraction axis. This eliminates the need for sample rotation or rastering, resulting in a highly stable and efficient imaging modality. We validated the efficacy of this approach through experimental imaging of an isolated twin domain within a bulk single crystal of an iron pnictide using a dark-field X-ray microscope. This advancement aligns with the enhanced brightness upgrades of modern synchrotron radiation facilities, unlocking new possibilities for high-resolution imaging of ordered materials.

Main

Dark-field X-ray microscopy (DFXM)[1] is a developing imaging technique for characterizing the micro- and mesoscale structural, electronic, and magnetic features of ordered materials in the form of single crystals, polycrystalline materials, and epitaxial thin films, with potential applications in artificial multilayers and quasicrystals. Unlike traditional transmission geometries, which rely on grating interferometry[2] or speckle scanning[3] to obtain dark-field or scattering signals, DFXM operates in Bragg geometry and utilizes a lens-based approach. This method employs diffracted X-ray Bragg peaks to generate real-space images that highlight structural heterogeneities visible through Bragg diffraction contrast[4], differentiating it from traditional in-line diffraction contrast techniques[5]. As a result, DFXM excels in isolating features such as structural twins, subtle charge and magnetic domain boundaries, interfaces between phases, small grains, and extended defects (e.g.

dislocations) in bulk matter, which are often impractical to image for other imaging modalities such as coherent diffraction imaging, electron microscopy or scanning tip methods[6].

Typically, DFXM employs an X-ray beam focused to sub-100 μm to illuminate a specific region in a sample oriented to excite a diffraction condition from a local grain, or domain, of interest. The Bragg diffracted beam passes through an X-ray objective and subsequently a magnified real-space intensity image is captured on a pixelated area detector, enabling diffraction-contrast images of the sample to be measured. The contrast stems from a plethora of structural factors, including variations in lattice orientation, scattering amplitude, and phase, as well as lattice strain, typifying the heterogeneities existing at various length scales in ordered materials. While the microscope with this arrangement can provide diffraction contrast in projected 2D images of the sample at a Bragg condition, transitioning from a 2D to 3D image generally requires rotating the sample

[1]Advanced Photon Source, Argonne National Laboratory, Lemont, IL, USA. [2]Department of Physics, Stanford University, Stanford, CA, USA. [3]Geballe Laboratory for Advanced Materials, Stanford University, Stanford, CA, USA. [4]Stanford Institute for Materials and Energy Sciences, SLAC National Accelerator Laboratory, Stanford, CA, USA. [5]Department of Physics, University of California, San Diego, CA, USA. [6]Institute of Microstructure Technology, Karlsruhe Institute of Technology, Karlsruhe, Germany. [7]Department of Applied Physics, Stanford University, Stanford, CA, USA. [8]Materials Science and Engineering Division, Argonne National Laboratory, Lemont, IL, USA. ✉e-mail: dgursoy@anl.gov; zahir@anl.gov

around a fixed momentum-transfer vector (Q) and solving the tomographic reconstruction problem to obtain a 3D image of the sample.

However, achieving accurate tomographic reconstruction requires extremely precise alignment of the sample around the Q vector to maintain the Bragg condition throughout the rotation. This demands rotation stages with minimal angular and translational runout, such as air-bearing stages, and a tedious manual alignment process. The reconstruction is further complicated by variations in the microscope's effective resolution function depending on the tomographic rotation angle[7]. Additionally, the effectiveness of geometry alignment algorithms for the lenses[8], or the sample[9] can be compromised if the incident beam intensity used for normalization is insufficient or fluctuates, or if the sample features change significantly at different incident angles near the Bragg peak. Due to these challenges, successful 3D reconstructions based on tomographic data remain scarce, with only one reported case to date[1].

An alternative to rotation-based methods is raster scanning with a thin beam (less than 1 μm) to map the sample volume. This technique relies on raster scanning of the sample, where the resolution depends on the focused beam size on the sample and the raster step. While this approach is computationally straightforward by eliminating the need for a full tomographic reconstruction, it is constrained by long collection times and potential instabilities associated with either rastering the sample or the focusing lens. Such instabilities can induce angular fluctuations that disrupt the Bragg condition, leading to significant degradation of spatial resolution in the scattering direction, particularly pronounced at small scattering angles. A method that employs a full beam without requiring sample movement could greatly enhance 3D DFXM by improving stability, reducing alignment time, and potentially enabling faster data collection.

In this paper, we propose leveraging a structured X-ray incident beam, as discussed in the case of optical light by Forbes et al.[10], as a robust and time-efficient alternative to conventional rotation-based DFXM for achieving 3D resolution. Structured light, widely utilized in diverse fields such as ghost imaging[11] and single-pixel cameras[12], involves projecting predetermined light patterns onto the sample and capturing variations in the reflected or transmitted light using a detector. Additionally, we investigate advancements in manufacturing X-ray modulators in the form of absorbing coded apertures at micron scales and evaluate their potential applicability in realistic length scales for DFXM. This structured illumination method maintains the sample in a fixed position, circumventing the instabilities associated with sample rotation and calibration to which we alluded above, imposing fewer restrictions on sample environments, making it well-suited for conducting in situ or *operando* imaging experiments at relevant resolutions with upgraded synchrotron sources. Additionally, it can facilitate imaging of plate-like samples, such as those in our study, which present challenges due to increased thickness at certain angles, resulting in artifacts similar to those seen in limited-angle tomography. However, it is important

to note that this method is susceptible to intensity fluctuations. Therefore, a stable beam or a method for monitoring beam intensity during scanning is required. To demonstrate the effectiveness of our approach, we apply it to the structural 3D imaging of the low-temperature orthorhombic phase of a single-crystal Ba $(Fe_{0.98}\ Cu_{0.02})_2As_2$ sample.
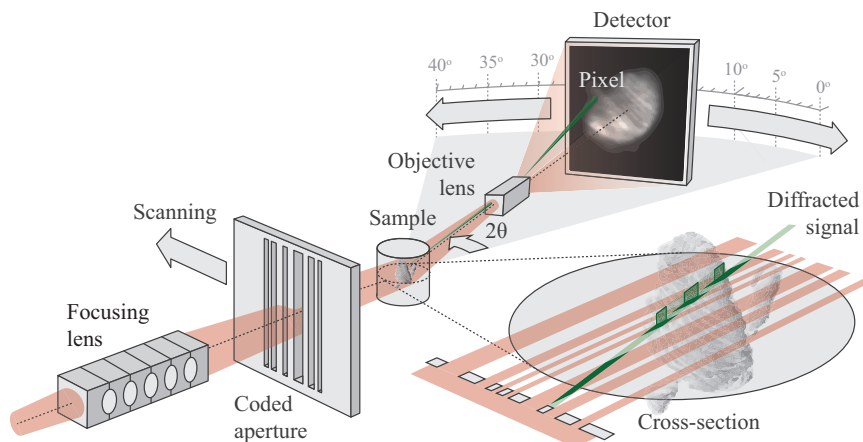
Results

Working principle

We illustrate a representative experimental setup demonstrating the application of micro-coded apertures for structuring illumination in DFXM in Fig. 1. A focused beam of illumination, ranging from about 10 to 100 μm in diameter, is directed toward a targeted volume within a crystalline sample. The goal is to achieve an X-ray beam sufficient in size so as to illuminate the entire volume of interest without scanning. In this context, a variety of X-ray optics options are available, ranging from capillaries to refractive lenses and mirrors. The real-space image of the illuminated volume projected to 2D undergoes magnification through an objective lens and is subsequently recorded by a pixel-array area detector positioned at a required imaging distance along and normal to a Bragg-diffracted beam. Selecting an objective lens with a numerical aperture typically around 0.0004 is crucial to reject other diffracted signals. CRL[13] or Fresnel zone plates[14] are excellent choices that offer this capability.

This setup captures a 2D image of the diffracting portions of the illuminated volume onto the detector. To achieve spatial resolution along the Bragg diffracted beam, we propose structuring the focused incident beam transversely to the incident-beam propagation and recording the modulation of intensity measurements in each detector pixel to a controlled change of the imposed structure in illumination. The aim is to encode depth information along the diffracted beam by modulating intensity and subsequently employ digital reconstruction techniques to decipher or decode the recorded intensities for each pixel.

However, structuring light in the hard X-ray regime poses significant challenges due to the fact that hard X-rays interact weakly with matter compared to visible or near-infrared light. As a result, our approach utilizes an X-ray-absorbing barcode-like structure with pseudo-random patterning as the aperture. This aperture is scanned normally to the beam to introduce diversity into the illumination, enabling depth (axial) resolution along the exit wave. Nanofabrication methods are available to produce micro-coded apertures of highly absorbing gold or tungsten structures ranging from 1 to 10 micrometers in thickness on a thin membrane. As we show, these micro-coded apertures can achieve the desired depth resolution of a few micrometers or less, approaching the sub-micrometer transverse resolution in the image plane in our present study.

The cross-section of the sample depicted in Fig. 1 offers an in-depth exploration of the model of DFXM with structured illumination. Here, the coded aperture imparts a distinct pattern to the X-ray beam before its

Fig. 1 | Experimental setup for 3D DFXM with structured illumination. A focusing lens directs the X-ray beam onto a selected crystalline grain or domain, while a 2D pixel-array detector captures its magnified image at the Bragg angle (2θ) via an objective lens. A scanning-coded aperture with an absorbing micro-pattern modulates the illumination for data collection from a fixed sample, enabling digital reconstruction of the grain's 3D structure. The cross-section of the sample is magnified to illustrate how a diffracted signal in a detector pixel responds to the internal diffraction (green boxcars) of a specific grain dictated by the selectively illuminated regions.

interaction with the crystalline sample. As a result, the response in a single pixel of a detector is set by diffraction occurring only at the locations marked in dark green. Essentially, the measurement at a detector pixel can be described linearly by the summation of all of those diffracting elements selected by the structured illumination. By systematically changing the coded aperture's position in known steps, we can generate a set of image measurements, each resulting from different patterns of illumination contributing to each pixel. This concept allows us to establish a system of linear equations that facilitates the determination of the diffraction profile within the grain along the direction normal to the DFXM image plane. This reconstruction process can be carried out independently for each detector pixel, thus providing a 3D image with a diffraction contrast mechanism dictated by the Bragg condition of the measurement.

In mathematical terms, structured illumination can be represented by the vector $a = [a_1, a_2, \ldots, a_L]^T$, with each coefficient describing the optical transmissivity of a given location of the coded aperture. Here, L is the number of components in a piecewise constant representation of the entire aperture. For example, a value of "0" indicates that an incident beam on the coded aperture can pass through without being absorbed, while "1" signifies complete absorption. In practice, these values often fall between 0 and 1, depending on factors such as the thickness and material of the coded aperture, as well as the energy and incidence angle of the X-ray beam.

Because the footprint of the X-ray beam on the aperture surface is smaller than the total aperture size, we used a smaller segment of the coded aperture, denoted as $a_p = [a_p, \ldots, a_{p+N-1}]^T$, to model the interaction of the beam with the aperture. This can be mathematically expressed through matrix multiplication as follows:

$$
\begin{bmatrix} d_1 \\ d_2 \\ \vdots \\ d_M \end{bmatrix} = \begin{bmatrix} a_p & a_{p+1} & \cdots & a_{p+N-1} \\ a_{p+1} & a_{p+2} & \cdots & a_{p+N} \\ \vdots & \vdots & \ddots & \vdots \\ a_{p+M-1} & a_{p+M} & \cdots & a_{p+M+N-2} \end{bmatrix} \begin{bmatrix} s_1 \\ s_2 \\ \vdots \\ s_N \end{bmatrix}, \quad (1)
$$

where $d = [d_1, d_2, \ldots, d_M]^T$ represents the intensity vector acquired from a single detector pixel, which we obtain by translating the coded mask M times, and $s = [s_1, s_2, \ldots, s_N]^T$ denotes the signal scattered from the sample at the Bragg angle and collected in this pixel. Note that N is an arbitrary number that we select and is often smaller than L to cover the segment of the aperture that is used in data acquisition. We can use matrix notation to express Eq. (1) more concisely:

$$
d = As, \quad (2)
$$

where A is the $M \times N$ coding matrix. Each row corresponds to a detector pixel at a scan point, representing the coded aperture's geometry at that moment. The complete matrix A encompasses the entire scanning process.

Accurate knowledge of A is essential for success and must be achieved through characterization of the structure before the experiment, along with its positioning during the scan. Various microscopy techniques, such as optical, electron, or X-ray microscopy, can be employed depending on the desired resolution. Once the aperture structure is known, its spatial positioning can be coarsely determined using DFXM in bright-field mode. Finer positioning is less critical when the aperture is normal to the incident beam, allowing minor misalignments to be disregarded at the targeted resolution in this paper. For higher resolutions, more precise calibration and tracking methods such as laser interferometry can be utilized. Additionally, encoder readings from the motorized scan help in tracking aperture positions during the experiment, and this information is directly incorporated into constructing the A matrix.

The corresponding image reconstruction problem can be formulated in the least-squares sense. Given the measured dark-field intensity data vector, denoted as d, and the system matrix, denoted as A, representing the linear relationship between the unknown signal vector, denoted as s, and the measured data, the problem can be written as:

$$
\min_s \| d - As \|_2^2 \quad (3)
$$

where $\| \cdot \|_2^2$ denotes the Euclidean norm. The system matrix (A) holds the relationship between the coded aperture pattern and the resulting scattered X-ray signals. The resolution of the reconstructed signal is closely related to the rank of the system matrix and how we solve the problem in Eq. (3). By solving this problem for each pixel in the detector, we can recover an image representation of the sample in the least-squares sense.

Validation on a twinned orthorhombic structure

We validated our technique by imaging the 3D low-temperature microstructure of a single crystal of Ba $(Fe_{0.98} Cu_{0.02})_2As_2$, commonly referred to as Cu-Ba122. Cu-Ba122 belongs to the 122 family of iron pnictides known to host many interesting electronic and magnetic properties such as electronic nematicity and unconventional superconductivity[15,16]. At room temperature, Cu-Ba122 possesses the tetragonal crystal structure of $ThCr_2Si_2$[17] and upon cooling to $T_S = 94 \pm 0.45$ K, it undergoes a structural phase transition from tetragonal to orthorhombic symmetry. This transition induces an orthorhombic distortion that causes atoms to shift along the tetragonal $(110)_T$ direction. Consequently, the primitive lattice vectors along the ab-plane in the orthorhombic phase experience a 45° rotation compared to those in the tetragonal phase, and their lengths become unequal ($a_O > b_O$). Additionally, the formation of orthorhombic twin domains below the phase transition leads to the splitting of the tetragonal $(220)_T$ peak into four peaks, each of which corresponds to a domain type, mirroring observations in the parent compound $BaFe_2As_2$[18,19].

We collected DFXM measurements at the 6-ID-C beamline of the Advanced Photon Source (APS) to capture the spatial structure of the domains resulting from this phase transition. During the measurements, we kept the sample below T_S at 6 ± 0.05 K in a low-vibration cryostat[20] and imaged the Bragg peak corresponding to one of the four orthorhombic domain types in a Laue horizontal diffraction geometry. We show the resulting DFXM images of a particular orthorhombic domain deeply embedded within the bulk crystal in Fig. 2. This initial data consists of a series of 2D DFXM images taken without a coded aperture. We fixed 2θ and mapped out the diffracting features of the twin domain in fine θ steps about the Bragg condition. A noteworthy feature of this particular domain is the presence of micron-scale spatial modulations in diffraction intensity. These modulations permeate throughout the image, and the axis of modulation is inclined by 45° with respect to the horizontal diffraction plane. Since the observed images are projections of the orthorhombic domain onto a 2D detector, the observed spatial contrast is indicative of the full 3D structure of the domain even if the images themselves lack depth resolution.

To achieve axial depth resolution, the collection of 3D data involved fixing 2θ, positioning θ, and scanning the coded aperture across the incident beam at a location 9.4 mm. Since resolution depends on the projected bit sizes at the sample's position rather than on distance alone, one could design a tailored aperture with bit sizes suited to the specific experimental configuration and constraints. Ranges of 2θ, θ, and aperture are detailed in the Data Collection section. We note that the angles (θ, 2θ) selected for coded aperture scans were more coarsely spaced compared to the 2D DFXM scan (see dark red marks in Fig. 2). For the coded aperture, we employed a binary barcode design composed of gold (Au) lines as shown in Fig. 3a, b. Scanning this coded aperture across the incident beam cast shadows of the Au lines on the sample and thus modified the scattering intensity captured by the detector pixels. Such a vertical shadow can be observed in the middle of the left image in Fig. 3c. Note that the detector image also displays a 45°–inclined modulation, which reflects intrinsic sample features distinct from those caused by the aperture.

Furthermore, the full shadow profile of the coded aperture can be viewed by plotting the intensity of the pixels along the yellow dotted line in Fig. 3c as a function of aperture scan position. The resulting plot shown in Fig. 3d displays slanted bar profiles that are indicative of the difference in the

Fig. 2 | Recorded diffraction images at different θ angles. Measured intensity plot versus the angle of incidence θ is obtained by integrating the images collected at the corresponding angle. The images captured without the coded aperture are recorded by incrementally stepping θ in increments of 0.003°, with the detector positioned at the Bragg angle (2θ). Fitting a Gaussian function to the Bragg peak reveals a mean of 11.374° and a standard deviation of 0.0055°.
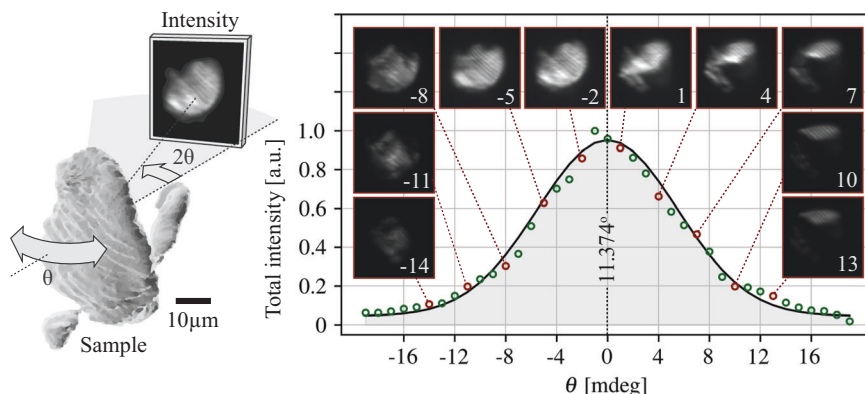
Fig. 3 | Depth estimation by scanning the coded aperture. a SEM image of the coded aperture, featuring a highlighted zoomed-in section to detail the bar lengths. Binary code sequence, where the orange line in (**a**) and (**b**) marks the bars used for encoding during data acquisition. **c** Representative single dark-field image, showing a recording with visible features. **d** Scanning image of the transverse plane, corresponding to the section of the image in (**b**) marked by the dotted yellow line. The vertical axis aligns with the direction along the dotted line, while the horizontal axis represents the scan steps of the coded aperture. Reference points (**a**, **b**, **c**) are marked for use in the subsequent plot (**e**), which illustrates their measurements obtained during the scanning of the coded aperture. Corresponding estimated values derived from depth-resolved signals are presented in (**f**).
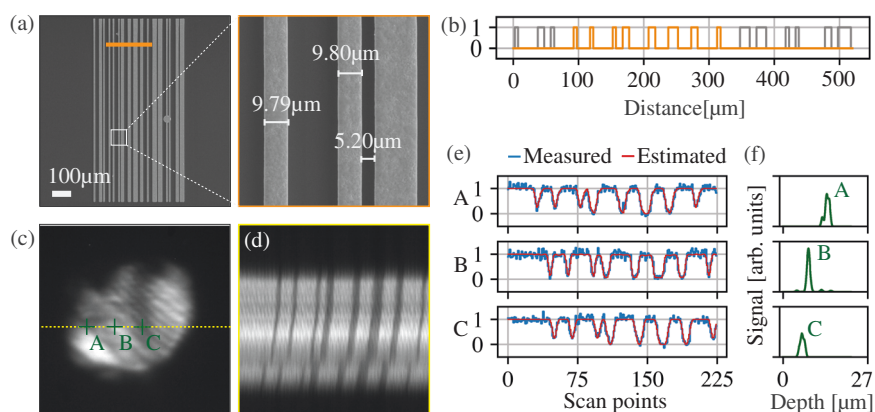
depth within the domain from which the corresponding scattering intensity emanates, providing visual evidence for the depth sensitivity allowed by the coded aperture method. Moreover, Fig. 3e depicts for three representative pixels the excellent agreement between the measured intensity and the estimated intensity as a function of scan position. The estimated intensity is derived from the depth-resolved signals resulting from the reconstruction process discussed above, and the agreement provides further quantitative corroboration of the depth sensitivity.

We present our results that capture the full 3D structure of the embedded orthorhombic domain in our Cu-Ba122 sample in Fig. 4. At several different near-Bragg diffraction conditions we imaged this domain in real space, here represented either as diffraction density cuts through the reconstruction (a) or as isosurfaces (b, c). These 3D reconstructed images enable us to observe that the 45°-inclined intensity modulations in the 2D images in Fig. 2 permeate through the depth of the domain. Similar modulations were seen in surface-sensitive optical measurements before in related compounds, and corresponding diffraction studies suggested that the modulations extend along the depth of the sample[18]. We expect these modulations to arise from local deviations from the average structure of the domain, and the related mechanism will be studied in future work. Here, we emphasize that our reconstructed images are in line with previous observations and also extend our understanding by elucidating the full 3D structure of the domain.

Further to note is the excellent angular resolution afforded by the low numerical aperture that allows us to differentiate disjointed regions scattering at the same (θ, 2θ) condition as can be seen in Fig. 4c. As (θ, 2θ) is varied, we see that there is a continuity in the regions coming in and out of the Bragg condition. The systematic comparison of the imaged 3D structures at different (θ, 2θ) values and their consistent evolution with respect to each other provides further confidence in the ability of our

coded aperture reconstruction process to achieve accurate depth resolution.

The scans performed in Fig. 4 allow us to construct a 3D composite map of the local lattice tilt in this embedded domain. After reconstructing the 3D structure for each angle θ at a fixed 2θ, we calculated for each voxel the center of mass value of the θ angle. As seen in Fig. 4c, as the tilt angle changes, different portions of the domain move into and out of Bragg conditions. The composite map of the center of mass of θ, *therefore,* covers the volume of the entire domain, leading to a larger imaged volume than a single tilt angle (see the difference in size of Fig. 4a compared with Fig. 5). This procedure provides the dominant lattice tilt at that selected spatial position and allows the creation of a 3D orientation map for the sample. The corresponding reconstructed lattice orientation is shown in Fig. 5. The slices indicated on the left panel reveal a spread of 0.02° of the tilt in the internal structure of the embedded orthorhombic domain (Fig. 5a–l). The shape of the domain and the gradients achieved from the composite center of mass images (Fig. 5) agree well with the observed changes in the domain from Fig. 4c. This continuous gradient of lattice tilts across the internal components of the domain provides further verification of this method.

Visualizing the spatial distribution of lattice tilt within a domain in 3D yields important information about its internal structure. In addition, our 3D method can be combined with different types of scans to probe a variety of structural properties, such as using a longitudinal scan to visualize the axial strain and its gradients within a domain in 3D. In sum, our results demonstrate the power of our depth-sensitive imaging technique to uncover deeply embedded structures on the mesoscale with nanoscale resolution.

Discussion

In this work, we have introduced a structured illumination approach to DFXM that enables 3D diffraction contrast imaging with a fixed sample and

detector geometry, designed for the investigation of crystalline samples. Our innovative technique replaces the traditional sample rotation or thin-beam slicing in existing DFXM methods with a scanning aperture featuring structured patterns. This advancement opens up exciting possibilities for the reconstruction of heterogeneous lattice structures within crystals with submicron 3D resolution. The potential of this method for revealing relevant local structures pertinent to crystalline materials in situ was shown via 3D reconstruction of a twin domain in Cu-Ba122 at cryogenic temperatures.

Our approach can also benefit various other X-ray microscopy techniques. For example, Laue micro-diffraction microscopy has already demonstrated the effective use of micro-coded apertures to expedite data collection times[21,22]. Likewise, diffraction imaging at grazing-incidence angles shares similarities, allowing for the manipulation of the diffracted beam through a coded aperture to either eliminate the need for rotations or reduce their frequency. However, it is worth noting that while this approach shows promise for these techniques, each of them does come with its specific experimental constraints that need to be considered and addressed.

For a widespread application of our approach as alluded to above we discuss potential future directions of handling the optimization problem outlined in Eq. (3). Although we employed a least-squares method, a better alternative approach could involve utilizing a regularized version of the problem[23]. Introducing a cost function that penalizes infeasible or unlikely solutions can offer a more effective foundation for compressive

sensing[24,25]. This could potentially result in accelerated data acquisition with a reduced requirement for capturing a large number of images. Depending on the availability of training data, we can also explore the potential benefits of employing supervised[26,27] or unsupervised[28] models based on deep neural networks. These models have the capacity to enhance both accuracy and reduce the number of required measurements and radiation dose, depending on the specific application. The signal reconstruction problem, implemented here, is addressed individually for each pixel intensity modulation profile resulting from the scanning of the coded aperture. As a result, the computational complexity of this method scales linearly with the quantity of detector pixels, making it amenable to parallel processing. This approach offers a direct avenue for harnessing the computational power of GPUs, which offer thousands of parallel processing units in contrast to CPUs. In terms of memory requirements, the method also scales linearly with the number of detector pixels; however, this demand can be partly facilitated by caching memory that is shared by all processors.

In this study, we introduced a coded aperture approach for stable 3D imaging without sample rotation, achieving detailed reconstructions while maintaining sample stability, which is particularly advantageous for complex or alignment-sensitive samples. This method enables full-field 3D views of structural properties, providing new insights into bulk phenomena such as charge density waves and magnetic phase competition, while also supporting rapid, low-dose data collection. Although optimizing the aperture's effects or resolution was beyond this study's scope, future research could focus on refining these aspects to increase its utility alongside existing diffraction-based techniques.

Looking forward, our approach and ongoing efforts include the development of non-attenuating or mixed-coded apertures that increase photon efficiency and support advanced encoding schemes through complex wave interactions. By utilizing both phase shifts and intensity modulation, these apertures allow for more refined manipulation of Bragg-diffracted signals, overcoming flux reduction limitations. This direction holds significant potential to expand DFXM in materials research, increasing its utility alongside existing diffraction-based methods to capture high-resolution 3D structural details and dynamic material behaviors.

Methods
Sample preparation
We grew the Cu-Ba122 crystal used in this work using a self-flux method[29,30]. The crystal grows as thick platelets, with the large face corresponding to the tetragonal ab-plane. The Cu doping level 0.02 ± 0.0008 of the batch was determined by electron probe microanalysis wavelength-dispersive spectroscopy (EPMA-WDS) using parent compound $BaFe_2As_2$ and Cu metal as calibration samples. We obtained the measured sample by cleaving it from a single crystal using a razor blade, and it had the dimensions $3.9 \times 1.4 \times 85 \, \mu m$.
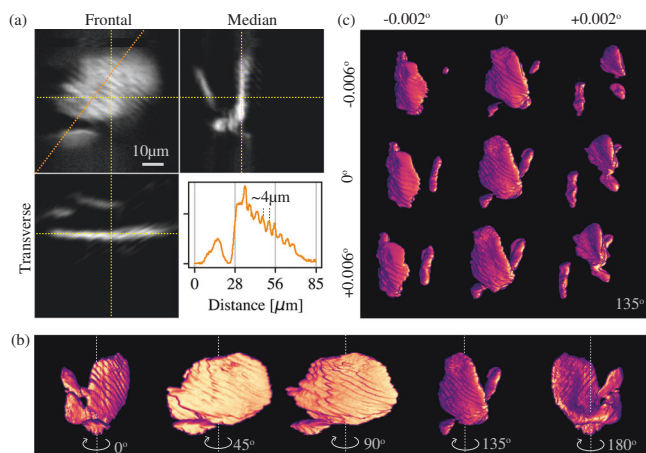
Fig. 4 | Reconstructed 3D volume of the imaged domain in the Cu-Ba122 sample. **a** Orthogonal planar view depicting the reconstructed 3D structure. The inset represents a profile along the orange-marked line in the frontal view. **b** Rendered perspectives of the 3D structure from various rotational angles. **c** Renderings illustrating the reconstructed 3D structures at a select of scattering ($\Delta(2\theta) = \mp 0.002°$) and rocking angles ($\Delta\theta = \mp 0.006°$). The middle image corresponds to the one displayed in (**b**).

Fig. 5 | 3D orientation reconstruction from rocking curve scanning. The frontal, transverse, and median planes on the left match the cuts shown in Fig. 4 for consistent orientation across figures. To provide a more comprehensive analysis of the crystal structure, additional slices (**a**–**l**) have been introduced. These cross-sectional views of the 3D sample show smooth and continuous structural variations throughout the sample, providing a consistent depth reconstruction.
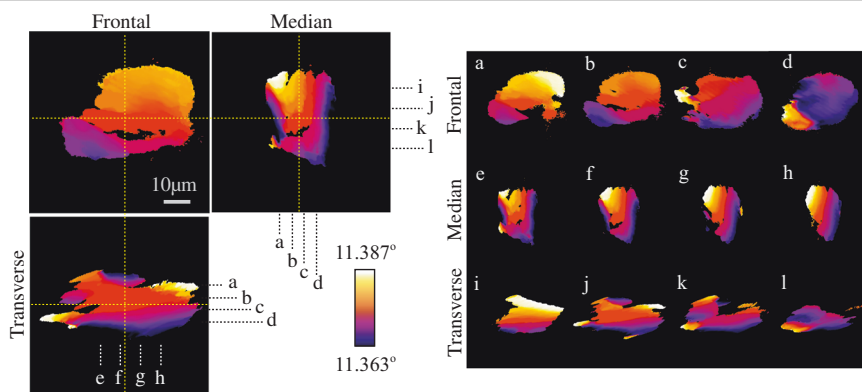
Dark-field X-ray microscope

At the 6-ID-C beamline of the APS, DFXM employed a CRL made of beryllium[31] as the focusing optics, achieving illumination of the volume of interest with a spot size of 50 μm on the sample. The setup incorporated a polymeric CRL[32] as an objective lens with a 131 mm focal length at 20 keV. The sample was placed 140 mm from the objective lens, experiencing an X-ray magnification of 24 incident upon a LuAG(Ce) scintillator crystal with a thickness of 20 μm. An optical imaging system was used to record the scintillator surface and provided an additional magnification of 5, leading to an overall magnification of 120. Consequently, we achieved a pixel size of 50 nm in the detector plane.

Coded aperture design and manufacturing

The pattern for the coded aperture was derived from a de Bruijn sequence of length 256 and order 8, providing uniqueness within each 8-bit long sequence. The fabrication of the coded aperture took place in the clean room at the Center for Nanoscale Materials at Argonne National Laboratory, utilizing direct-write lithography and electroplating. It featured a 5 μm wide Au for the 1-bits and a 10 μm wide silicon nitride (Si_3N_4) membrane with negligible absorption for the 0-bits. Thickness measurements along the optical axis indicated an approximate thickness of 5 μm using a scanning electron microscope and scanning profilometer.

Data collection

We positioned the coded aperture 9.4 mm upstream of the sample, as close to the sample as could be achieved before contacting the outer vacuum shroud of our cryostat. This configuration ensures that the barcode footprint of the coded aperture projects onto the sample. The aperture was scanned perpendicular to the incident beam direction within the horizontal scattering plane in increments of 1 μm steps for a total scan range of 225 μm. The translation stage used demonstrated positional stability down to 30 nm. The motor encoder accurately tracked these positions, which were utilized in the subsequent image reconstruction. The exposure of the detector was 0.5 ms at each coded aperture step scan location.

We collected a matrix of coded aperture scanning measurements at ten different sample incident angles from $-0.014°$ to $0.013°$ in steps of $0.003°$ from $(040)_o$ Bragg peak condition, and three different scattering angles, $-0.003°$, $0°$, and $0.003°$ from Bragg peak 2θ of this twin domain. This measurement generated thirty datasets, with each dataset comprising 225 images.

Sample reconstruction

We performed digital sample reconstruction from the acquired data using custom in-house software. This software solves the optimization problem described in Eq. (3) and employs the non-negative least squares method[33], implemented in SciPy[34]. The effective resolution is calculated to be 0.45 μm for the raw projection images and 0.49 μm for the 3D reconstruction along the scattering angle, based on the Fourier Ring Correlation with half-bit measurement, as implemented in ImageJ[35]. To construct the system matrix (**A**), we utilized the actual positions of the coded aperture based on the encoder readings of the high-precision linear stage used for aperture translation. The reconstruction took several hours on a commercial laptop without parallelization or code optimization. Currently, we are finalizing the software repository but can provide the code, scripts, and data upon request.

References

1. Simons, H. et al. Dark-field X-ray microscopy for multiscale structural characterization. *Nat. Commun.* **6**, 6098 (2015).
2. Pfeiffer, F. et al. Hard-X-ray dark-field imaging using a grating interferometer. *Nat. Mater.* **7**, 134–137 (2008).
3. Wang, H., Kashyap, Y. & Sawhney, K. Hard-X-ray directional dark-field imaging using the speckle scanning technique. *Phys. Rev. Lett.* **114**, 103901 (2015).
4. Jakobsen, A. et al. Mapping of individual dislocations with dark-field X-ray microscopy. *J. Appl. Crystallogr.* **52**, 122–132 (2019).
5. Davis, T. J., Gao, D., Gureyev, T., Stevenson, A. & Wilkins, S. Phase-contrast imaging of weakly absorbing materials using hard X-rays. *Nature* **373**, 595–598 (1995).
6. Yildirim, C., Cook, P., Detlefs, C., Simons, H. & Poulsen, H. F. Probing nanoscale structure and strain by dark-field X-ray microscopy. *MRS Bull.* **45**, 277–282 (2020).
7. Poulsen, H. F. et al. X-ray diffraction microscopy based on refractive optics. *J. Appl. Crystallogr.* **50**, 1441–1456 (2017).
8. Breckling, S. et al. An automated approach to the alignment of compound refractive lenses. *Synchrotron Radiat.* **29**, 947–956 (2022).
9. Gürsoy, D. et al. Rapid alignment of nanotomography data using joint iterative reconstruction and reprojection. *Sci. Rep.* **7**, 11818 (2017).
10. Forbes, A., de Oliveira, M. & Dennis, M. R. Structured light. *Nat. Photonics* **15**, 253–262 (2021).
11. Shapiro, J. H. Computational ghost imaging. *Phys. Rev. A* **78**, 061802 (2008).
12. Duarte, M. F. et al. Single-pixel imaging via compressive sampling. *IEEE Signal Process. Mag.* **25**, 83–91 (2008).
13. Snigirev, A., Kohn, V., Snigireva, I. & Lengeler, B. A compound refractive lens for focusing high-energy X-rays. *Nature* **384**, 49–51 (1996).
14. Gorelick, S. et al. High-efficiency fresnel zone plates for hard X-rays by 100 kev e-beam lithography and electroplating. *J. Synchrotron Radiat.* **18**, 442–446 (2011).
15. Paglione, J. & Greene, R. L. High-temperature superconductivity in iron-based materials. *Nat. Phys.* **6**, 645–658 (2010).
16. Fernandes, R. M. et al. Iron pnictides and chalcogenides: a new paradigm for superconductivity. *Nature* **601**, 35–44 (2022).
17. Rotter, M., Tegel, M. & Johrendt, D. Superconductivity at 38 k in the iron arsenide (ba 1 - x k x) fe 2 as 2. *Phys. Rev. Lett.* **101**, 107006 (2008).
18. Tanatar, M. et al. Direct imaging of the structural domains in the iron pnictides a fe 2 as 2 (a = ca, sr, ba). *Phys. Rev. B* **79**, 180508 (2009).
19. Blomberg, E. et al. Effect of tensile stress on the in-plane resistivity anisotropy in bafe 2 as 2. *Phys. Rev. B* **85**, 144509 (2012).
20. Plumb, J. et al. Dark field X-ray microscopy below liquid-helium temperature: the case of namno2. *Mater. Charact.* **204**, 113174 (2023).
21. Gürsoy, D., Sheyfer, D., Wojcik, M., Liu, W. & Tischler, J. Z. Depth-resolved Laue microdiffraction with coded apertures. *J. Appl. Crystallogr.* **55**, 1104–1110 (2022).
22. Gürsoy, D., Sheyfer, D., Wojcik, M., Liu, W. & Tischler, J. Z. Digital autofocusing of a coded-aperture Laue diffraction microscope. *Rev. Sci. Instrum.* **94** 013702 (2023).
23. Gürsoy, D. et al. Maximum a posteriori estimation of crystallographic phases in X-ray diffraction tomography. *Philos. Trans. R. Soc. A Math. Phys. Eng. Sci.* **373**, 20140392 (2015).
24. Donoho, D. L. Compressed sensing. *IEEE Trans. Inf. Theory* **52**, 1289–1306 (2006).
25. Candès, E. J., Romberg, J. & Tao, T. Robust uncertainty principles: exact signal reconstruction from highly incomplete frequency information. *IEEE Trans. Inf. Theory* **52**, 489–509 (2006).
26. Yang, X. et al. Low-dose X-ray tomography through a deep convolutional neural network. *Sci. Rep.* **8**, 2575 (2018).
27. Liu, Z. et al. Tomogan: low-dose synchrotron X-ray tomography with generative adversarial networks: discussion. *J. Optic. Soc. Am. A* **37**, 422–434 (2020).
28. Ulyanov, D., Vedaldi, A. & Lempitsky, V. Deep image prior. In *Proc. IEEE Conference on Computer Vision and Pattern Recognition* 9446–9454 (IEEE, 2018).

29. Chu, J.-H., Analytis, J. G., Kucharczyk, C. & Fisher, I. R. Determination of the phase diagram of the electron-doped superconductor ba (fe 1- x co x) 2 as 2. *Phys. Rev. B* **79**, 014506 (2009).

30. Ni, N. et al. Temperature versus doping phase diagrams for ba (fe 1- x tm x) 2 as 2 (tm = ni, cu, cu/co) single crystals. *Phys. Rev. B* **82**, 024519 (2010).

31. Qiao, Z. et al. A large field-of-view high-resolution hard X-ray microscope using polymer optics. *Rev. Sci. Instrum.* **91**, 113703 (2020).

32. Nazmov, V. et al. Fabrication and preliminary testing of X-ray lenses in thick su-8 resist layers. *Microsyst. Technol.* **10**, 716–721 (2004).

33. Lawson, C. L. & Hanson, R. J. *Solving least squares problems* (SIAM, 1995).

34. Virtanen, P. et al. SciPy 1.0: fundamental algorithms for scientific computing in Python. *Nat. Methods* **17**, 261–272 (2020).

35. Nieuwenhuizen, R. P. et al. Measuring image resolution in optical nanoscopy. *Nat. Methods* **10**, 557–562 (2013).

Author contributions

Z.I. and D.G. designed the project, and D.G. wrote the code and performed the reconstructions. M.W. and A.L. fabricated the optics. K.A.Y. and E.K. analyzed the results. K.A.Y., E.K., D.G., M.H., D.S., S.H., Z.I., and I.R.F. contributed to the interpretation of the results. All authors contributed to the discussions. D.G. wrote the manuscript. All authors contributed to the review of the manuscript.

Competing interests

The authors declare no competing interests.

Additional information

Correspondence and requests for materials should be addressed to Doğa. Gürsoy or Zahir Islam.

Peer review information *Communications Physics* thanks Hugh Simons and the other, anonymous, reviewer(s) for their contribution to the peer review of this work.

Reprints and permissions information is available at http://www.nature.com/reprints

Publisher's note Springer Nature remains neutral with regard to jurisdictional claims in published maps and institutional affiliations.